



Impedance and modulus analysis of barium calcium titanate ferroelectric ceramics

Satyanarayan Patel¹ · Lalitha Kodumudi Venkataraman² · Harekrishna Yadav¹

Received: 2 September 2020 / Revised: 9 November 2020 / Accepted: 11 November 2020 / Published online: 3 December 2020
© The Korean Ceramic Society 2020

Abstract

BaTiO₃-based derivatives have been explored in recent times for potential applications in energy harvesting and ultrasonics. To this end, energy harvesting and conversion applications require an understanding of the conduction and loss mechanisms. The conduction mechanism in Ba_{0.9}Ca_{0.1}TiO₃ (BCT) ceramics is studied using impedance spectroscopy at different temperatures. Impedance analysis suggests the presence of two types of relaxation processes corresponding to grain and grain boundary contributions. The relaxation mechanism follows non-Debye-type behavior. The high resistance of the grain (bulk) in the ferroelectric region does not contribute to the high losses; the losses probably result from the phase transition. In addition, BCT ceramics exhibit a negative temperature coefficient of resistance (NTCR). The open-circuit pyroelectric voltage shows a twofold increase compared to (Ca, Zr) modification in BaTiO₃.

Keywords Lead free · BCT ceramics · Impedance spectroscopy · Electric modulus

1 Introduction

Oxide ferroelectrics are pertinent for their potential applications in different electronic devices such as transducers, precision actuators, multilayer capacitors, computer memory, tunable microwave mixers, delay lines, filters, and phase shifters for steerable antennas [1–4]. In this purview, lead zirconium titanate, Pb(Zr,Ti)O₃-based materials exhibit unique ferroelectric, piezoelectric, and pyroelectric properties that have led them to dominate the market for several decades [5–7]. However, Pb(Zr,Ti)O₃ constitutes 60–70% lead, which is toxic to the environment and health during the fabrication process of the material and disposal of the device components [8]. Therefore, there is an urgent need to develop lead-free piezoelectric materials that can be used as alternatives to PZT [8]. In this direction, four categories of lead-free materials are currently being

investigated—BaTiO₃, (Na_{1/2}Bi_{1/2})TiO₃, (K_{0.5}Na_{0.5})NbO₃ and BiFeO₃ based [9]. These belong to the ABO₃-type perovskite family with excellent piezoelectric and ferroelectric properties. The fabrication of (Na_{0.5}Bi_{0.5})TiO₃, (K_{0.5}Na_{0.5})NbO₃ and BiFeO₃-based materials are difficult due to the volatile and hygroscopic nature of their component elements and they also exhibit high leakage currents [9]. In comparison, BaTiO₃ (BT)-based materials are easy to fabricate and scale the production process, and they exhibit lower leakage currents and poling fields. Although, BT-based perovskites have been extensively explored in the past for high strain actuating applications and multilayer capacitors, recent research has identified newer, impending application areas in energy harvesting, ultrasonic applications such as transducers and high voltage supply transformers [4]. Therefore, apart from realizing potential applications from existing BT-based materials, efforts are directed towards developing new BT-based compositions.

Recently, Ca-substituted BaTiO₃ ceramics were demonstrated to exhibit very high pyroelectric and piezoelectric properties [10–12]. Ba_{1-x}Ca_xTiO₃ compositions are identified to be the most effective materials for thermal energy harvesting or pyroelectric applications [10, 13]. Ba_{0.9}Ca_{0.1}TiO₃ (BCT) exhibits a pyroelectric voltage of 10 V when a heating cycle of 6 K/s is used at room temperature [10]. BCT is also explored for the piezocatalytic

✉ Satyanarayan Patel
spatel@iiti.ac.in

¹ Discipline of Mechanical Engineering, Indian Institute of Technology Indore, Indore, Madhya Pradesh 453 552, India

² Department of Materials and Earth Sciences, Technical University of Darmstadt, 64287 Darmstadt, Hessen, Germany

and photocatalytic de-colorization of a typical dye molecule methyl orange [14]. In the same way, it can also be used in pyrocatalysis, and water treatment applications can be thrust areas of research apart from the thermal energy harvesting [15]. For the various pyroelectric-based applications, surface charge generation is crucial. Hence, the A-site cation (Ca) substitution in BaTiO_3 plays a vital role in the polar behavior, conductivity and dielectric relaxation process [11, 12, 16]. The conduction mechanism and loss present in the BCT can significantly alter the pyroelectric properties. Therefore, this work aims to investigate the dielectric dispersion and conduction mechanism in BCT ceramics using impedance spectroscopy.

In view of this, $\text{Ba}_{1-x}\text{Ca}_x\text{TiO}_3$ ($0.2 \leq x \leq 0.3$) synthesized by mechanochemical methods were investigated. The effect of Ca substitution was correlated to dielectric permittivity and impedance analysis at 675–805 K [16]. Further, resistance degradation behavior of $\text{Ba}_{1-x}\text{Ca}_x\text{TiO}_3$ ($x \leq 0.1$) and $\text{Ba}(\text{Ti}_{1-y}\text{Ca}_y)\text{O}_3$ ($0 \leq y \leq 0.015$) was investigated by the Warburg impedance analysis in the temperature range of 448–623 K. [17]. Moreover, dielectric relaxation analysis of $\text{Ba}_{1-x}\text{Ca}_x\text{TiO}_3$ ($x = 0.0\text{--}0.3$) at room temperature (0–2.5 MHz) reveals that the local lattice distortion assists in pinning the electric dipole and consequently reduces the relaxation time (Ca is ≤ 14 at%) [11]. A non-Debye-type dielectric relaxation was observed for $\text{Ba}_{0.8}\text{Ca}_{0.2}\text{TiO}_3$ and the conduction was attributed to doubly ionized oxygen vacancies $V_{\text{O}}^{\bullet\bullet}$, while the relaxation was proposed to be of dipolar nature [18]. Investigation of complex impedance and modulus properties in BaTiO_3 , $\text{Ba}_{0.9}\text{Ca}_{0.1}\text{TiO}_3$, La-doped BaTiO_3 and La-doped BCT was performed in a frequency range of 40 Hz–1 MHz and temperature range of ambient–500 °C [19]. The grain and grain boundary contributions were established via dielectric plots; however, grain and grain boundary contribution and associated relaxation processes were not clearly discerned in the impedance and modulus plots [19]. In the laser-ablated thin film of $\text{Ba}_{0.9}\text{Ca}_{0.1}\text{TiO}_3$, the activation energy of 1.05 eV was evaluated from impedance spectroscopy, which was attributed to the oxygen vacancy mobility [20]. However, the effect of grain and grain boundary, relaxation process and conductivity analysis is not discussed. Some of the Zr-substituted $\text{Ba}_{1-x}\text{Ca}_x\text{TiO}_3$ compositions, such as $\text{Ba}_{1-x}\text{Ca}_x\text{Zr}_{0.1}\text{Ti}_{0.9}\text{O}_3$ ($0.00 \leq x \leq 0.20$), were investigated in detail for the resistance behavior of the grain (bulk) and the grain boundary, activation energy, electric modulus and conductivity behavior [21]. Similarly, in $\text{Ba}_{0.85}\text{Ca}_{0.15}\text{Zr}_{0.1}\text{Ti}_{0.9}\text{O}_3$ ceramics, impedance analysis and dielectric relaxation behavior were also performed over the wide frequency (0.1 Hz–1 MHz) and temperature range (273–973 K) [22, 23]. Most previous studies focused on other modified compositions like $\text{Ba}(\text{Ti}_{1-y}\text{Ca}_y)\text{O}_3$ and $\text{Ba}_{1-x}\text{Ca}_x\text{Zr}_{0.1}\text{Ti}_{0.9}\text{O}_3$ rather than BCT.

Until now, a detailed analysis of the relaxation and conductivity mechanism of undoped BCT between 353–853 K in the frequency range of 0.1 Hz–3 MHz has not been undertaken, which is crucial to comprehend the potential energy harvesting and catalysis applications, as stated previously. Therefore, a detailed analysis is performed with complex impedance (Z^*) and electric modulus (M^*) by employing an equivalent circuit model. Two relaxations were identified in the frequency range of 0.1 Hz–3 MHz at high temperatures. Further, resistance and capacitance for grain and grain boundary were estimated. Finally, the pyroelectric performance is exemplified by an open-circuit voltage measurement.

2 Materials and methods

Polycrystalline $\text{Ba}_{0.9}\text{Ca}_{0.1}\text{TiO}_3$ (BCT) was fabricated by the mixed-oxide route. Stoichiometric ratio of reagent grade powder of BaCO_3 , CaO and TiO_2 (purity $\geq 98.5\%$) was weighed and mixed thoroughly using ball milling in acetone medium. The resultant powder was calcined at 1300 °C/4 h and again ground. The ground powder was mixed with 2 wt. % polyvinyl alcohol as a binder, using a mortar and pestle and uniaxially pressed with the help of hydraulic press into discs of about $1.5 \times 11 \text{ mm}^2$ (thickness \times diameter). The green sample was sintered at 1480 °C/5 h in air. X-ray diffraction (XRD) (Rigaku Smart Lab, Japan) was employed to verify the phase purity of the sintered sample. The microstructure was obtained using a scanning electron microscope (SEM) (FEI SEM NOVA Nanosem 450, Hillsboro, OR) from a sintered pellet after grinding and cleaning the surface in an ultrasonic bath using acetone. The density of sintered samples was measured by the Archimedes method. The sintered sample was ground to make plane parallel surface and sputtered with silver for electrical characterization. Temperature-dependent polarization-electric field (P-E) loops were recorded with the help of a modified Sawyer Tower circuit (Marine India) at 50 Hz. The dielectric properties were measured in the temperature range of 300–450 K at various frequencies using an LCR meter (Agilent E4990A, Agilent Technologies Inc., Santa Clara, CA). For the dielectric measurement, a ramp rate of 2 °C/min and a square sample of $7.12 \times 7 \text{ mm}^2$ was used. Impedance spectroscopy (IS) measurements were done using an Alpha-A impedance analyzer (Novocontrol Technologies, Montabaur, Germany) at 0.1 V. The sample used for IS measurement was 1.34 mm thick and 10.7 mm in diameter. The IS analyses were performed in the frequency range of 0.1 Hz–3 MHz from 353 to 633 K. The recorded IS data were analyzed using RelaxIS software (RHD instruments, Marburg, Germany).

3 Results and discussion

3.1 Structural and microstructural analyses

Figure 1a presents the room temperature XRD of the sintered pellet sample of BCT. The XRD pattern was indexed using the previously reported literature [12]. It confirms the successful formation of a pure perovskite phase of BCT ceramics. Figure 1a confirms that no secondary phase is observed within the instrument detection limits. The SEM micrograph recorded for the sintered pellet is presented in Fig. 1b, indicating high density of the sintered sample. The density was also measured by the Archimedes method and the relative density of the final sample is $\sim 94\%$. It also confirms that the sintered sample is free from any major porosity. The average grain size estimated using Image-J software is found to be $8.7 \pm 0.35 \mu\text{m}$. The statistical summary of grain size diameter of ceramics is shown in the inset of Fig. 1b.

3.2 Ferroelectric and dielectric analyses

Figure 1c depicts the P-E hysteresis loop of BCT at different temperatures. BCT exhibits the typical ferroelectric behavior with a well-saturated hysteresis loop at room temperature (303 K). The ferroelectric loops are almost linear (paraelectric phase) at 423 K, presenting a normal ferroelectric behavior upon heating. To find the exact ferroelectric (FE)–paraelectric (PE) phase transition temperature, permittivity (ϵ) versus temperature is presented in Fig. 1d in 100 Hz–1 MHz frequency range. It is observed that ϵ increases with increasing temperature and attains a maximum value of 8000. A sharp peak around 400 K corresponds to the structural phase transformation from tetragonal to cubic, attributed to the FE–PE phase transition. Due to the difference in the Ba^{2+} and Ca^{2+} ionic radius, it was proposed that a diffuse, frequency-dependent permittivity response may occur close to the Curie temperature (T_C) [11]. However, the lower Ca^{2+} dopant concentration in this work does not significantly affect Curie temperature and the nature of phase transition. Further, T_C does not shift with frequency which indicates that BCT belongs to traditional ferroelectrics but not relaxor, as also evident from the P–E loops in Fig. 1c. Dielectric loss

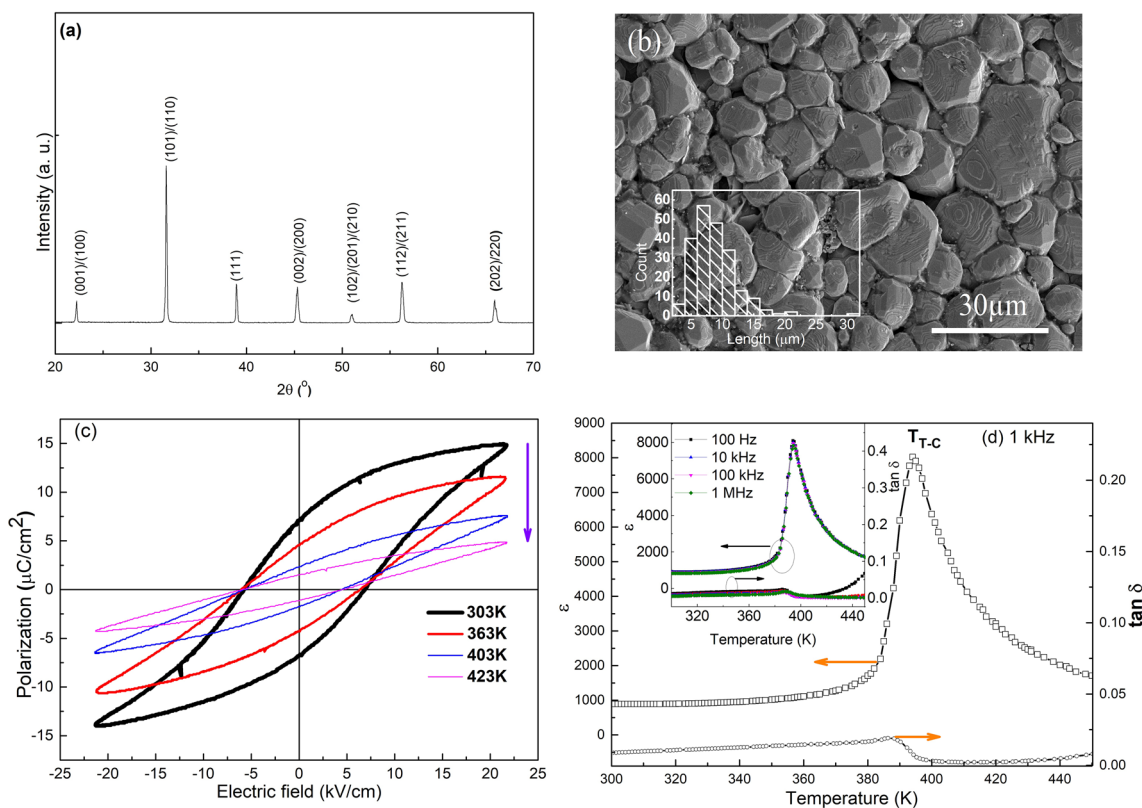


Fig. 1 **a** X-ray diffraction spectra of BCT measured at room temperature, **b** SEM micrograph of the sintered sample; inset depicts the statistical distribution of grain size, **c** P-E loops at a different tempera-

ture, **d** dielectric constant (ϵ) and loss ($\tan\delta$) versus temperature at a frequency of 1 kHz [15]. Inset shows ϵ and $\tan\delta$ versus temperature plots at various frequencies

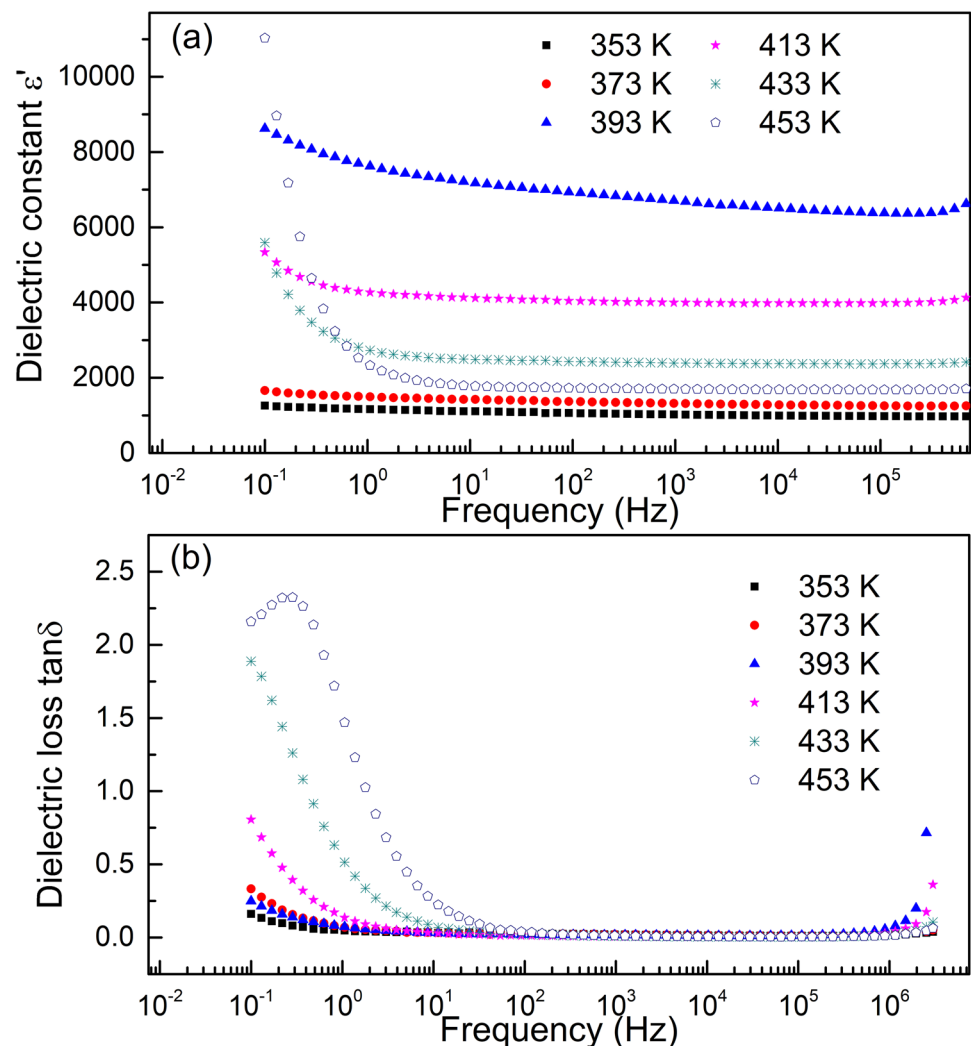
($\tan\delta$) increases with temperature until T_C (400 K) and then decreases drastically. $\tan\delta$ starts to increase again above 430 K. The temperature- and frequency-dependent permittivity and $\tan\delta$ are depicted in Fig. 2a, b. The investigated temperature range is limited to 353–453 K, keeping in mind the practical application point of view dictated by T_C .

Figure 2a presents that a higher value of ϵ' is observed in the lower frequency region at all temperatures. ϵ' decreases with increasing frequency due to the electric dipole's inability to comply with the variation of applied ac electric field. ϵ' increases with the applied temperature up to T_C (as also observed in Fig. 1d) and then starts to decrease due to structural phase transition, which is typical behavior of ferroelectric based dielectric materials. Further, two different regions are observed in ϵ' plot: a strong dispersion in lower frequency region (see 453 K) and a plateau region in the high frequency regime. ϵ' remains unchanged at high frequency due to the release of associated space charge [24]. $\tan\delta$ (Fig. 2b) also exhibits a similar trend. The higher values of ϵ' and $\tan\delta$ show the effect of space charge polarization

and/or conducting ion motion. Polycrystalline oxide ferroelectrics constitute several interfaces such as domain boundaries, grain boundaries and oxide-electrode interface. Such interfaces possess large interfacial energy and these are ideal sites for defects due to their lower potential energy. When defects are trapped in such interfaces, it results in a buildup of space charge. Because of the difficulty in recovery from these traps, space charges are generated at the interfaces in the material.

The large value of ϵ' can be related to charge accumulation at the sample and electrode interfaces such as space charge polarization [24]. However, the higher value of $\tan\delta$ at low frequencies is the effect of the free charge motion within the materials. Further, the significant drop in $\tan\delta$ (see 453 K) with frequency indicates the role of conductivity and space charge polarization on the ferroelectric relaxation process. Hence, dielectric dispersion in the lower frequency region can be an effect of the polarization mechanism accompanying the thermally activated conduction of mobile ions and/or other defects [24].

Fig. 2 Frequency dependence of **a** dielectric constant (ϵ') and **b** loss ($\tan\delta$) at various temperatures



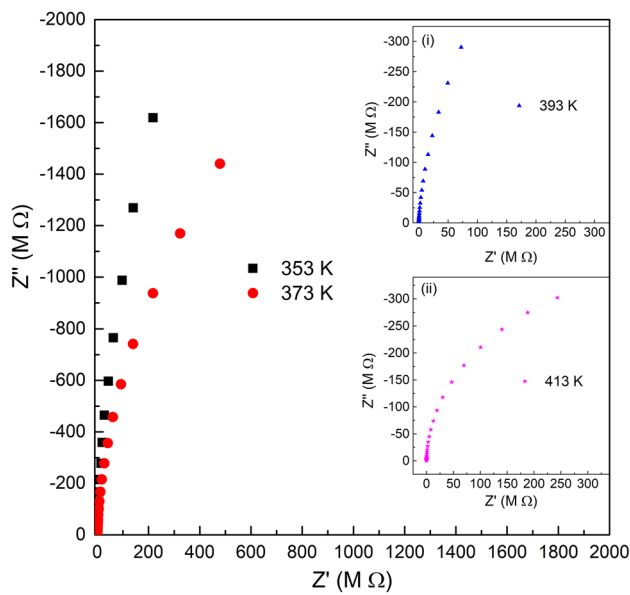


Fig. 3 Complex impedance plots of the real part (Z') versus imaginary part (Z'') for BCT at 353 K and 373 K. Insets shows the complex impedance spectra at (i) 393 K and (ii) 413 K

3.3 Impedance spectroscopy

To understand the observed dielectric dispersion behavior, impedance analysis was undertaken. Figure 3 presents the complex impedance spectra (Nyquist plots) at temperatures 353–413 K over the frequency range 0.1 Hz–3 MHz. The linear trend of Z' (real part) versus Z'' (imaginary part) in the range 353–393 K indicates the insulating behavior. As the temperature increases above 393 K (inset Fig. 3(i)), it starts to gradually change into a single semicircular arc (process) at 413 K and above (inset Fig. 3(ii)). Each semicircular response corresponds to a single process (contribution from grain, grain boundary, or electrode interface). The complete first semicircular arc can be resolved at 433 K (inset Fig. 4a). Further, at and above 473 K, the single arc can be resolved into two overlapping semicircles (not shown here). Figure 4 depicts two overlapping semicircles at 513 K. If the temperature is further increased to 573 K or above, three processes can be discerned (inset Fig. 4b). These semicircles can be characterized by two (at 513 K) and three (at 573 K) equivalent circuit parallel RQ elements in series, where R and Q are the resistance and constant phase element of the circuit, respectively. The arc starts from the origin and centers of the semicircles lie below the x -axis, illustrating a non-Debye relaxation process. Therefore, it cannot be fitted very well with an ideal capacitor (C) in parallel; hence Q is used as [25, 26]

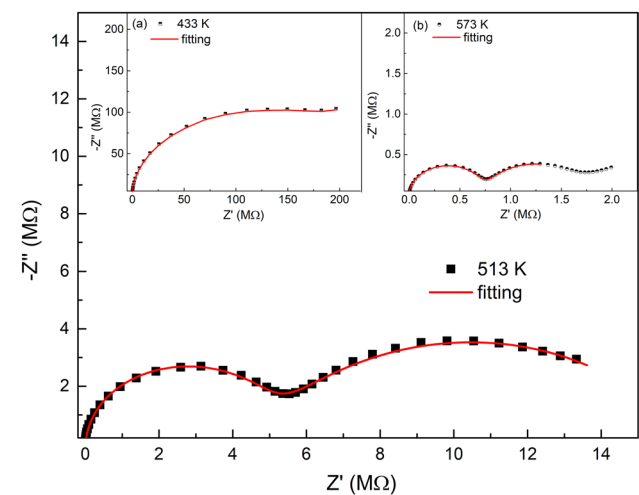


Fig. 4 Nyquist plot at 513 K along with the fits (solid line). Inset shows the Nyquist plot at **a** 433 K and **b** 573 K with the corresponding fits (solid line) [15]

$$Z_Q^* = \frac{1}{(i\omega)^\alpha C}, \quad (1)$$

where α is the empirical exponent and lies between 0 and 1; for an ideal capacitor and resistor $\alpha = 1$ and $\alpha = 0$, respectively.

Resolving these two arcs confirms that BCT consists of two relaxation process up to 513 K. However, as temperature increase > 533 (573 K), three relaxation processes can be observed. Generally, in most electroceramics, the semicircle at high frequencies reflects the bulk response, whereas the low-frequency region has contributions from the grain boundary [27]. However, the third semicircular process results due to the resistive response of the sample/electrode interface. Generally, peak frequency of the grain boundary response is significantly lower than that of the bulk (grain) response; this is because of their large C and R [25]. A parallel RQ circuit represents these arcs as individual components of the material. The intercept on the Z' axis is used to obtain the bulk resistance grain contribution. In contrast, the highest point in each semicircle is used to determine the capacitance of the sample. The solid line shows the best fitting an equivalent circuit model of RQ in parallel with the experimental data points in Fig. 4. The obtained parameters such as grain boundary resistance (R_{gb}), capacitance (Q_{gb}), relaxation time (τ_{gb}) and grain/bulk relaxation time (τ_{bulk}), resistance (R_{bulk}), capacitance (Q_{bulk}) are given in Table 1. BCT exhibits high R_{gb} in comparison with R_{bulk} at elevated temperatures. This can be an effect of low oxygen vacancy concentration and trapped electrons at the grain boundaries [23, 28]. A detailed discussion on the oxygen vacancy generation or other charge carriers and its conduction mechanism is discussed in [29]. However, in the ferroelectric region,

Table 1 Fitting parameter of resistance (R), capacitance (C) and relaxation time (τ) for the bulk and grain boundary of BCT ceramic

Temp (K)	Bulk/Grain				Grain boundary				Relaxation time	
	R_{bulk} (M Ω)	Q_{bulk} (pF)	n	C_{bulk} (pF)	R_{gb} (M Ω)	Q_{gb} (pF)	n	C_{gb} (pF)	τ_{bulk} (ms)	τ_{gb} (ms)
352	18,677.61	739	0.97	999	–	–	–	–	18,655,426	–
365	8674.06	855	0.96	1203	–	–	–	–	10,435,659	–
374	6058.72	967	0.96	1409	–	–	–	–	8,535,427	–
394	1816.05	5031	0.95	6768	–	–	–	–	12,291,255	–
414	730.55	2982	0.92	4630	–	–	–	–	3,382,727	–
434	215.10	1840	0.95	2385	–	–	–	–	512,978	–
453	83.87	1703	0.89	2602	–	–	–	–	218,264	–
473	27.11	1132	0.96	1271	67.73	30,257	0.74	37,265	34,464	2,524,076
493	10.53	838	0.98	892	24.69	39,018	0.73	34,560	9393	853,388
513	4.77	625	1	628	11.52	49,536	0.69	31,733	2998	365,689
533	2.40	582	0.98	600	4.61	55,763	0.76	30,410	1441	140,214
573	0.72	480	0.97	485	1.09	69,057	0.78	27,790	348	30,158
593	0.40	407	0.98	407	0.60	94,347	0.74	24,737	162	14,925
613	0.24	381	0.98	378	0.32	107,603	0.74	23,617	90	7578
633	0.15	352	0.98	346	0.18	131,889	0.73	21,968	51	4024

BCT exhibits very high R_{bulk} . From Table 1, it is clear that mainly R_{bulk} dominates up to 453 K. In contrast, both R_{gb} and R_{bulk} are present above 453 K. Similar behavior was also observed in $\text{Ba}_{0.85}\text{Ca}_{0.15}\text{Zr}_{0.1}\text{Ti}_{0.9}\text{O}_3$ ceramics by Rafiq et al. [22]. R_{gb} and R_{bulk} decreases with increasing temperature, indicating a negative temperature coefficient of resistance (NTCR) in the BCT ceramics. The capacitance C_{gb} is found to be almost two orders higher than C_{bulk} , and exhibits similar trends with temperature as observed for R .

Table 1 indicates that relaxation time τ_{bulk} and τ_{gb} decreases with increasing temperature, and the Arrhenius plots of τ_{bulk} and τ_{gb} are plotted in Fig. 5a following the equation [24, 30]:

$$\tau = \tau_0 \exp \frac{E_{\text{relx}}}{k_{\text{B}} T}, \quad (2)$$

where τ is the relaxation time, τ_0 is the relaxation time at infinite temperature, E_{relx} denotes the activation energy for the relaxation process, T is the absolute temperature and k_{B} is the Boltzmann constant. Arrhenius data fitted using the Eq. (2) are displayed in Fig. 5a. These slopes were used to calculate the grain and grain boundary relaxation activation energies as ~ 1.13 eV and ~ 1.03 eV, respectively, as displayed in Fig. 5a. It is evident from the relaxation activation energies that both processes can be attributed to the same nature of charge carrier process due to small differences in their activation energy. Figure 5a also presents the bulk (grain) activation energy in ferroelectric and paraelectric regions, which is found as 0.41 and 1.13 eV, respectively. The large difference in the activation energy between the ferroelectric and paraelectric regime indicates that the surface polarization significantly alters the relaxation process.

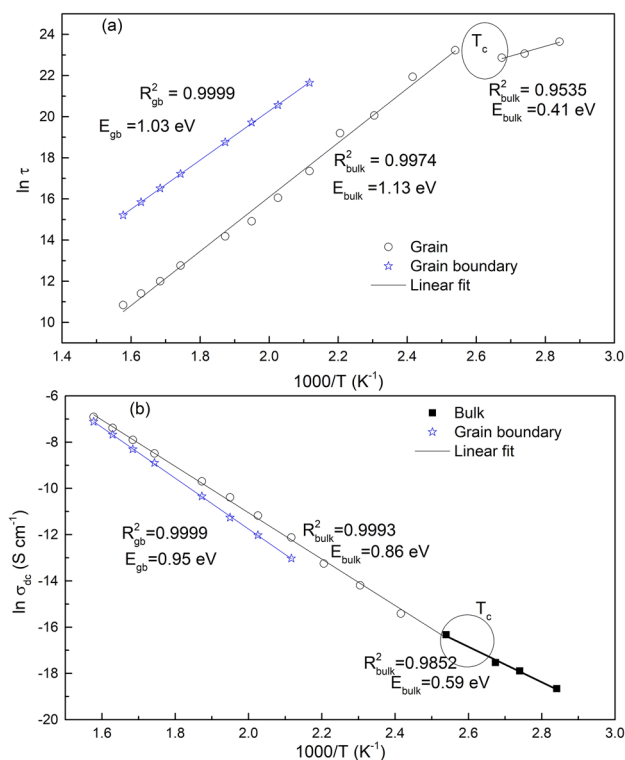


Fig. 5 a Relaxation time (τ) versus the inverse of temperature and b variation of dc conductivity (σ_{dc}) with the inverse of temperature plots for grain and grain boundary of BCT ceramics [15]. R^2 denotes the goodness-of-fit

Figure 5b presents the Arrhenius plots of σ_{dc} . The slope of the Arrhenius plot varies near T_{C} , suggesting that the samples may exhibit different conduction mechanisms in the

ferroelectric and paraelectric regions. The thermally activated σ_{dc} also obeys the Arrhenius behavior, according to [31]

$$\sigma_{dc} = \sigma_0 \exp\left(-\frac{E_a}{k_B T}\right), \quad (3)$$

where E_a is the activation energy and σ_0 is a pre-exponential factor for dc conductivity. The activation energy of grain and grain boundary is determined by the slope of $\ln \sigma_{dc}$ versus $1/T$ plot for the electrical conduction processes. The activation energy for σ_{dc} is obtained as ~ 0.86 eV and ~ 0.95 eV for bulk and grain boundary processes, respectively. The difference in activation energy for bulk and grain boundary was also observed in prior reports [18, 23, 24]. The obtained activation energies are close to the oxygen vacancy conduction ~ 1 eV (as calculated for many perovskite systems). It suggests that in BCT ceramics, the conductivity process is mostly governed by the oxygen vacancies. The obtained result for the mobility of oxygen vacancies is consistent with the previous report for thin film $\text{Ba}_{0.88}\text{Ca}_{0.12}\text{TiO}_3$ [20]. The

small difference in activation energy (~ 0.09 eV) shows that both grain and grain boundary have a similar conduction process with a low potential barrier. Further, σ_{dc} activation energy for the grain is found to be 0.59 and 0.86 eV in ferroelectric and paraelectric regions. This implies that the motions of charge carriers are varied in these regions.

Figure 4 suggests that BCT has two processes discernable at elevated temperatures; hence, a closer look shall be taken on these distinct processes. Figure 6a presents Z' with frequency plots in the temperature range of 363–823 K with a temperature interval (ΔT) of 30 K. With increasing temperature, the magnitude of Z' decreases in the low-frequency region and confirms the NTCR behavior (Fig. 6a). Further, at high temperatures, it exhibits almost frequency-independent behavior up to a certain frequency. At low temperatures (ferroelectric region), it depends on the frequency and decreases rapidly with increasing frequency (Fig. 6a). Moreover, at higher frequencies, all the Z' curves tend to merge and indicate temperature-independent behavior. This may be attributed to the possible release of space charges [28, 32].

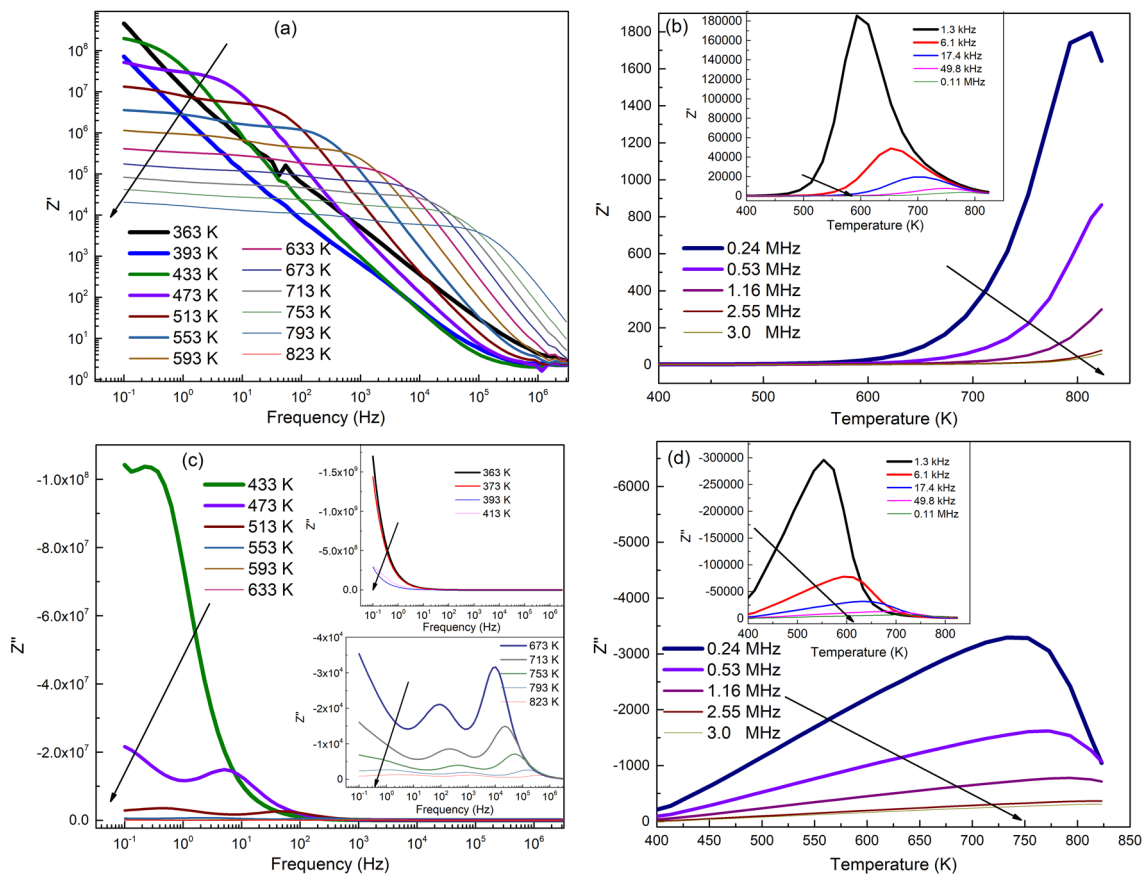


Fig. 6 **a** Real part (Z') of impedance as a function of frequency at a different temperature, **b** Z' versus temperature in the frequency range of 0.24 MHz to 3 MHz (inset shows 1.3 kHz to 0.11 MHz plots), **c** frequency-dependent variation of imaginary part (Z'') between 433

and 633 K (inset shows plots for a temperature range of 363 K–413 K and 673 K–823 K), **d** Z'' versus temperature in the frequency range of 0.24 MHz to 3 MHz (inset shows 1.3 kHz to 0.11 MHz plots). Arrow points to increasing temperature

Figure 6b shows the Z' versus temperature plots for 0.24–3 MHz frequency range. Inset of Fig. 6b presents similar plots for 1.3 kHz–0.11 MHz frequency range. Z' decreases with increasing frequencies near the peak temperature. The peak temperature shifts to higher temperatures with increasing frequency. These effects can be attributed to the defect concentration and charge accumulation at the grain boundaries [23].

Figure 6c illustrates Z'' with frequency at temperatures between 433 and 633 K with 30 K intervals. The insets of Fig. 6c show Z'' versus frequency plots for temperatures of 363–413 K and 673–823 K. The Z'' plots depict two relaxation peaks in the temperature range of 433–633 K and the height of the relaxation peaks decreases with the increase of temperature. The two relaxation peaks are attributed to the grain and grain boundary effects. Moreover, a significant broadening of Z'' peaks with temperature variation illustrate that BCT electrical processes are spread over different relaxation time. Figure 6d presents the Z'' as a function of temperature at different frequencies and the inset shows similar plots for 1.3 kHz–0.11 MHz. The Z'' peak shifts to the higher temperatures with a broadened response and decreases in magnitude with increasing frequency, suggesting the distribution of relaxation times, which is also evident from the asymmetric broadening of Z'' peaks. Z'' exhibits a decreasing trend with increasing frequency, attributed to space charge effects [23, 25]. Further, Z'' plots tend to merge at very high temperatures and frequency and the temperature and frequency-independent behavior in this region is plausibly due to the release of space charge [23]. At higher temperatures, electrical conduction can be attributed to various defects or vacancies apart from the space charge effects, via hopping of electrons or oxygen vacancies/defects among the available localized sites in the materials [24].

Generally, thermally activated relaxation processes in ceramics follow the Arrhenius law, as given in the Eq. (3). τ can be calculated from the frequency at which the maximum value of Z'' is obtained. At the peak, relaxation can be expressed as $\omega_p \tau_p = 1$, where τ_p is the relaxation time at the peak and $\omega_p = 2\pi f$. The relaxation frequency also obeys the Arrhenius relation and can be defined by [24]

$$\omega_p = \omega_0 \exp \left(-\frac{E_{\text{relx}}}{k_B T} \right), \quad (4)$$

where ω_0 is a pre-exponential factor. The NTCR characteristics of BCT renders an increasing trend for ω_p with increasing temperature, as shown in Figs. 3, 5 and 6a. This can be rationalized to result from oxygen vacancies [23, 33]. Relaxation parameters ω_0 and E_{relx} are obtained by plotting $\ln(\omega_p)$ versus $(1/T)$ data and fitted with Eq. (4), as shown in Fig. 7. The calculated activation energies are ~ 1.12 eV and ~ 1.0 eV for grain and grain boundary, respectively. The obtained values closely correspond to that determined by

τ (Fig. 6a). Thus, the same explanation is also valid for ω_p plots and obtained activation energy.

3.4 Modulus spectroscopy

Impedance data can be studied effectively using the complex modulus $M^*(\omega)$ plots based on the polarization analysis. The modulus spectroscopy plots are typically useful to study the real dielectric relaxation process when the two materials have similar resistance but exhibit different capacitance or very small differences in their capacitance. Another advantage compared to impedance analysis is that the $M^*(\omega)$ formulation can easily discriminate the difference between electrode polarization and grain boundary conduction. Therefore, due to these reasons, $M^*(\omega)$ formalism is considered to distinguish the effects separately. The complex electric modulus $M^*(\omega)$ in term of real (M') and imaginary (M'') parts can be expressed as

$$M^*(\omega) = M'(\omega) + jM''(\omega) = i\omega C_0 Z^*(\omega). \quad (5)$$

Complex electric modulus M^* studies have been carried out in the temperature range of 433–633 K ($\Delta T = 20$ K). Figure 8a, b depict variation of real (M') and imaginary (M'') parts of electric modulus versus frequency plots, respectively at 433–633 K ($\Delta T = 20$ K). Inset of Fig. 8a, b presents the M' and M'' as a function of frequency for 353–413 K (in ferroelectric region). M' exhibits almost frequency-independent behavior above 1 Hz in ferroelectric region. A dispersion mechanism until a certain frequency (0.1–1 Hz at 373 K) can be due to the short-range mobility of charge carriers. It is evident from Fig. 8a that M' approaches to 0

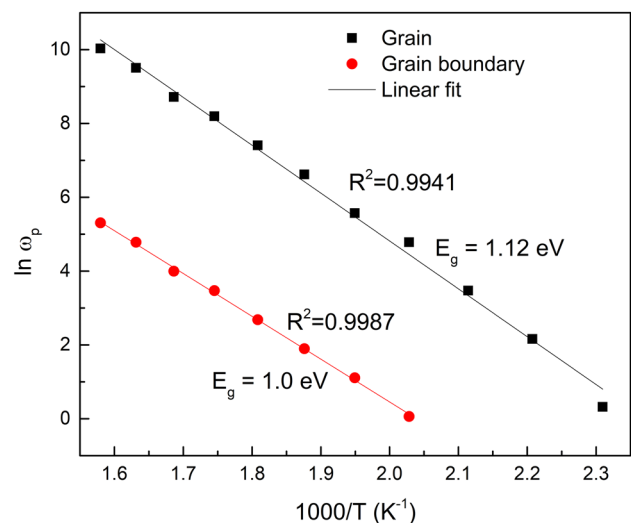


Fig. 7 Arrhenius plots of $\ln \omega_p$ (relaxation frequency) with inverse of temperature for grain and grain boundary process of BCT. R^2 denotes the goodness-of-fit

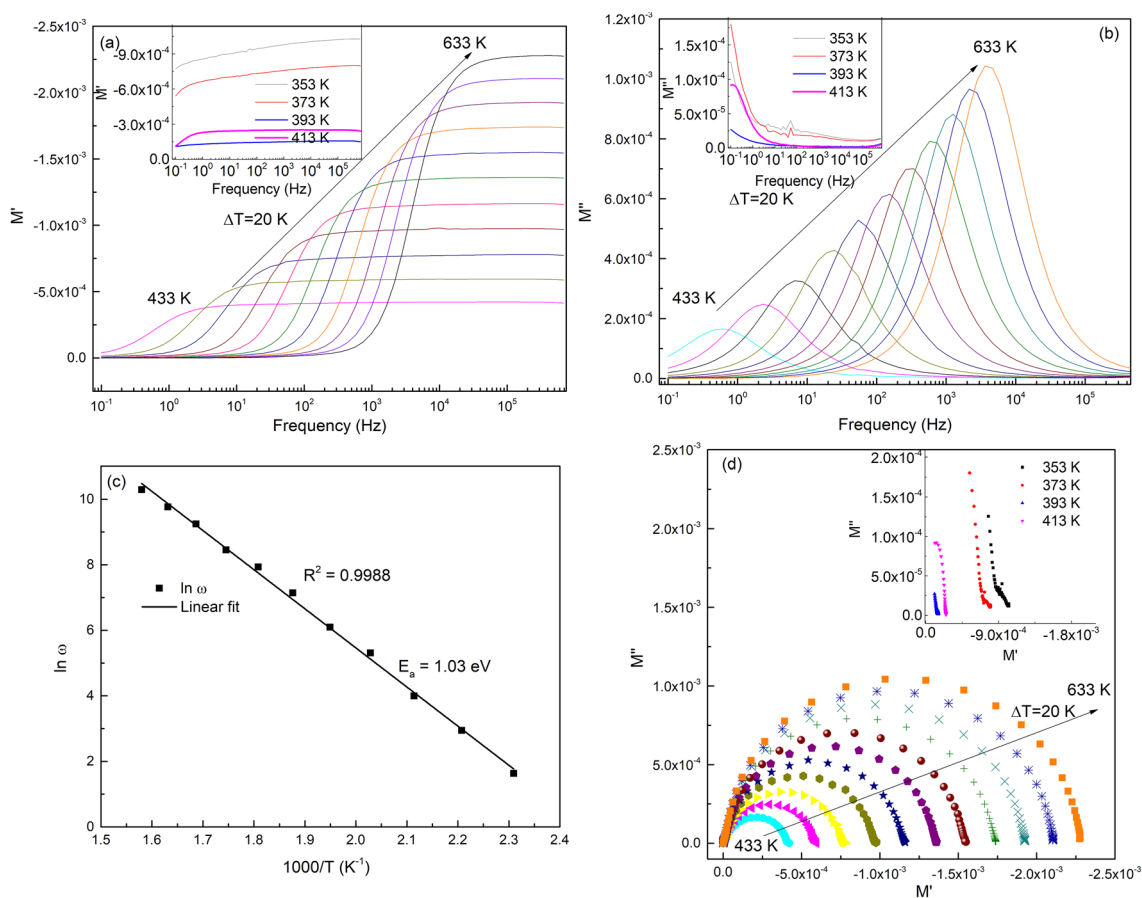


Fig. 8 **a** Real part (M') of modulus versus frequency between 433–633 K in the interval of 20 K (inset shows plots for 353 K to 413 K), **b** frequency-dependent variation of imaginary part (M'') of modulus between 433 K and 633 K with an interval of 20 K (inset

depicts plots for 353 K to 413 K), **c** variation of (maximum frequency obtained from the **b**) $\ln \omega$ with the inverse of temperature, **d** M'' versus M' at various temperatures (inset shows plots for 353 K to 413 K). R^2 denotes the goodness-of-fit

at lower frequencies. However, values of M' increases from the low frequency towards a high frequency. Moreover, M' consists of a dispersion which shifts to high frequency with increasing temperature. M' is almost constant at frequencies above ~ 10 kHz. These results suggest the presence of considerable electrode and/or ionic polarization in the temperature range of investigation. The increase in M' with increasing temperature confirms the temperature-dependent relaxation processes. This is rationalized due to the decrease in the capacitance with increasing temperature, a typical characteristic feature of ferroelectric materials above T_C (in the paraelectric phase) [23]. However, the dispersion in the M' peaks shifts to the high frequency regime with increasing temperature, indicating long-range mobility of charge carriers. Such behavior has also been observed for BZT–BCT compositions [23].

Inset of Fig. 8b shows that the M'' decreases in the ferroelectric region (353–413 K). The peak in M'' is not clearly observed in this region; however, it can be expected that it may follow the same trend as observed at 433 K

(paraelectric). Figure 8b reveals that, as the temperature increases, peak values of M'' also increases and shifts to a higher frequency. It suggests a decrease in associated capacitance value with temperature. M'' exhibits increasing trends with frequency, attains a peak value at a particular frequency, and then tends to decrease with a further increase in frequency. The smaller value of M'' at low frequency is due to a lack of electrode polarization mechanism. The curve's asymmetry behavior at peak shows the contribution of structural aspects and lattice defects in the conductivity [23]. At lower frequencies below the peak frequency, the charge carriers are mobile over a long distance. However, at frequencies above the peak frequency, the charge carriers are confined (due to potential well) and are mobile only over shorter distances. This validates the frequency-dependent short-range and long-range conduction mechanisms. Also, peak shift of M'' towards higher frequencies with temperature confirm the thermally activated behavior of the relaxation time. The peak frequency can be used to calculate the relaxation time (τ) as [30]

$$\tau = \frac{1}{\omega} = \frac{1}{2\pi f_r}, \tag{6}$$

where f_r is the frequency value at the peak position of M'' depicted in Fig. 8b. The activation energy determined by $\ln \omega$ versus $1/T$ plots using the Arrhenius Eq. (6) is presented in Fig. 8c. It is found to be ~ 1.03 eV, which is close to that obtained for τ -plot and σ_{dc} , hinting that the relaxation and conductivity processes are attributed to the same type of charge carrier.

The Nyquist plot of M' versus M'' is displayed in Fig. 8d for the temperature range 433–633 K. Inset depicts M' versus M'' plots for 353–413 K. The presence of single semicircles (arc) indicates bulk (grain) process only. However, impedance plots reveal two processes for grain and grain boundary effect, which is not very clear in the modulus plot. It is well known that the modulus plots are dominated by the smallest C components, whereas impedance plots are dominated by the largest R components. The C for grain and grain boundary given in Table 1 reveals that C_{gb} is two orders higher than that of C_g . This suggests that the capacitance effect

dominates the electric behavior at high temperatures. Thus, it is expected that only one semicircle arc is observed in electric modulus plots. The detailed analysis of a single arc and associated phenomenon are discussed for BZT–BCT ceramics by Kaushal et al. [23]. The obtained arcs are not perfect semicircle(s); the arcs center is below the M' -axis (X -axis). It suggests non-Debye type of relaxation process. The intercepts of arcs on M' axis shift towards the higher values of M' with increasing temperature, further elucidating the NTCR behavior.

Figure 9a presents the variation of Z'' and M'' plots with frequency at 473 K and 573 K (inset). Inset of Fig. 9a reveals that Z'' has two overlapped peaks at 573 K whereas M'' consists a broad peak in the higher frequency. M'' does not shows the low-frequency peak due to omega factor. This type of Z'' and M'' plot helps to determine if the bulk response arises due to long-range conductivity or localized relaxation [34, 35]. If Z'' and M'' peaks overlap, then it probably results from long-range conductivity, whereas separate peaks of Z'' and M'' reveals that the material exhibits its localized conduction mechanism due to multiple carriers

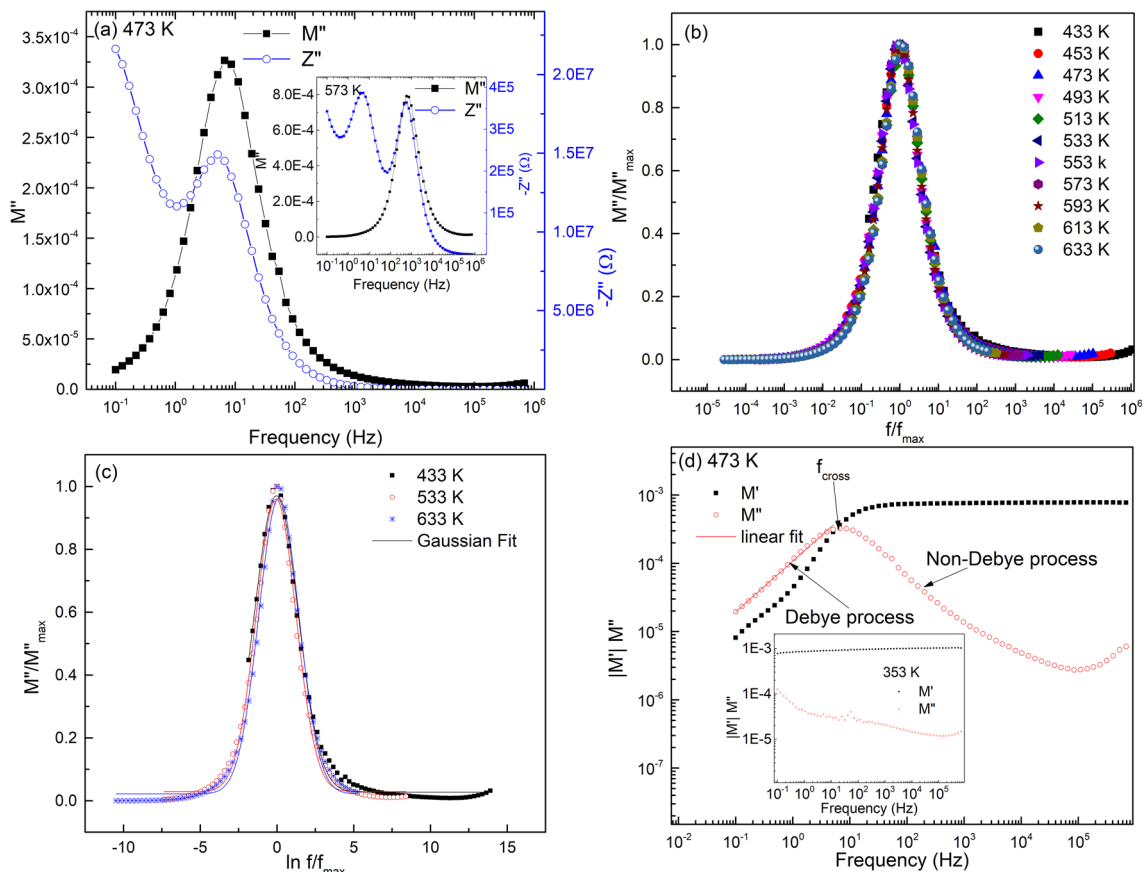


Fig. 9 a Variation of M'' and Z'' measured at 473 K (inset shows at 573 K), b Normalized imaginary parts M''/M''_{max} of modulus with frequency at a different temperatures, c M''/M''_{max} versus frequency

at different temperatures with corresponding fits, d M' and M'' , versus frequency obtained at 473 K. The frequency of the crossing point, f_{cross} indicates the σ_{dc} relaxation time

and relaxation processes. Z'' and M'' peaks are overlapping at higher frequency (grain component), signifying that the oxygen vacancies contribute to the dc conductivity at these temperatures.

Figure 9b, c presents the normalized modulus M''/M''_{\max} versus f/f_{\max} plots of the BCT at different temperatures. Figure 9b reveals that all the M''/M''_{\max} versus f/f_{\max} plots overlap with each other with almost similar shape and full width at half-maximum (FWHM) in the given temperature range. Further, the overlapping of plots shows that the dynamical process is nearly temperature independent. Moreover, the asymmetry of M''/M''_{\max} curve displays a non-exponential type of conductivity relaxation behavior. The normalized modulus plot with non-exponential decay function is given as [36]:

$$\emptyset(t) = \exp(-t/\tau)^\beta \quad (0 < \beta < 1), \quad (7)$$

where β is the Kohlrausch parameter; β decreases for increase in the distribution of relaxation time. The $\emptyset(t)$ and modulus relation in the given frequency range is expressed by [37]

$$M^* = M_s \left[1 - \int_0^\infty \exp(-i\omega t) \left(\frac{-d\emptyset(t)}{dt} \right) dt \right], \quad (8)$$

where $\lim_{\omega\tau \gg 1} M' = M_s$. β can be obtained as $\beta = 1/\text{FWHM}$. β indicates the deviation from the Debye-type relaxation process. If the value of β is smaller, larger the deviation from the Debye-type relaxation process. Further, β is also used to interpret the effects of correlated motions between ions. Figure 9c shows the Gaussian fit of M''/M''_{\max} versus f/f_{\max} plots at various temperatures which are used to calculate the FWHM. The FWHM is obtained as 3.34, 3.05 and 3.07 for temperatures of 433 K, 533 K and 633 K, respectively and corresponding β is determined as 0.299, 0.328 to 0.326. The obtained values of FWHM and β are comparable with the previous work on Cobalt sulfide and $20\text{CdI}_{2-80}[\text{xAg}_2\text{O} - \text{y}(0.7\text{V}_2\text{O}_5 - 0.3\text{B}_2\text{O}_3)]$ ionic materials [34, 37]. Further, FWHM is wider than the breadth of a Debye peak (1.14 decade), which supports that BCT exhibits a non-Debye type of relaxation process.

Figure 9d shows the $|M'|$ and M'' variation with frequency at 473 K and 353 K (inset). At lower frequencies, M'' follows a Debye-like process as depicted in Fig. 9d by the fits of solid lines. The maximum value of M'' provides the relaxation time of the dominant process. The most prominent relaxation process happens more broadly compared to a simple Debye relaxation process. However, it is not clear why this relaxation process is broad. One possible reason is a single peak originating from a broad distribution of relaxation times, because of the multiple energy barriers due to local defects [30]. f_{cross} , defined as the frequency of the crossing

point, is associated to the dc-conductivity relaxation time. Here, the maximum peak position f_{\max} and f_{cross} of $|M'|$ and M'' are the same. It indicates that the relaxation time dependence does not deviate from the Arrhenius behavior.

3.5 AC conductivity

The complex modulus and impedance analysis suggest that BCT exhibits short-range conduction. Further, dielectric analysis (Fig. 2) exhibits a high value of ϵ' and $\tan \delta$ reflecting the effect of space charge polarization and/or mobility of conducting ion within the material and is connected to ac conductivity relaxation. The ac conductivity (σ_{ac}) is determined using the following relation [34]

$$\sigma_{\text{ac}} = \frac{d}{A} \frac{Z''}{Z'^2 + Z''^2}. \quad (9)$$

Figure 10a, b presents σ_{ac} versus frequency curves at various temperatures. Figure 10a represents the effect of conductivity in the ferroelectric phase and Fig. 10b in the paraelectric phase. σ_{ac} increases with increasing frequency irrespective of applied temperature because of the charge carrier dispersion via oxygen vacancy or hopping. Apart from the frequency-independent plateau, two dispersion regimes are also present in the σ_{ac} plot, as shown in Fig. 10c. Region II (lower frequency) reflects the grain boundary contribution and region III (higher frequency) is associated with the grain contribution. Further, Fig. 10b shows a plateau of σ_{ac} at low frequencies i.e. frequency-independent conductivity values at a particular temperature that corresponds to the σ_{dc} . The conductivity displays non-linearly increasing behavior with increasing frequency and exhibit dispersion at higher frequencies. It is the result of a drastic increase in charge carrier mobility that reflects an increase in conductivity [38]. The dispersion occurs at the hopping frequency (ω_{H}) of the material, at which more active charge carriers hop from one site to another

Figure 10d depicts the thermal behavior of σ_{ac} at different frequencies (0.1 Hz–1 MHz). σ_{ac} sharply increases with temperature and an anomaly has been observed at a particular temperature. The obtained change in slope corresponds to the phase transition temperature, which reflects the change in the conductivity phenomenon in paraelectric and ferroelectric regions, indicating a strongly temperature-dependent conductivity response. At higher temperatures, the onset of intrinsic conductivity occurs and dominates the conduction mechanism. The activation energy can be calculated from the slope of the plots (Arrhenius equation fitted for σ_{ac} using Eq. 3). The activation energy of σ_{ac} is obtained as 0.70 and 0.46 eV for 0.1 Hz and 100 Hz, respectively in the ferroelectric region. The activation energy is 0.80, 0.76, 0.75, 0.66, 0.39 and 0.11 eV at 0.1 Hz, 100 Hz, 1 kHz, 10 kHz, 100 kHz

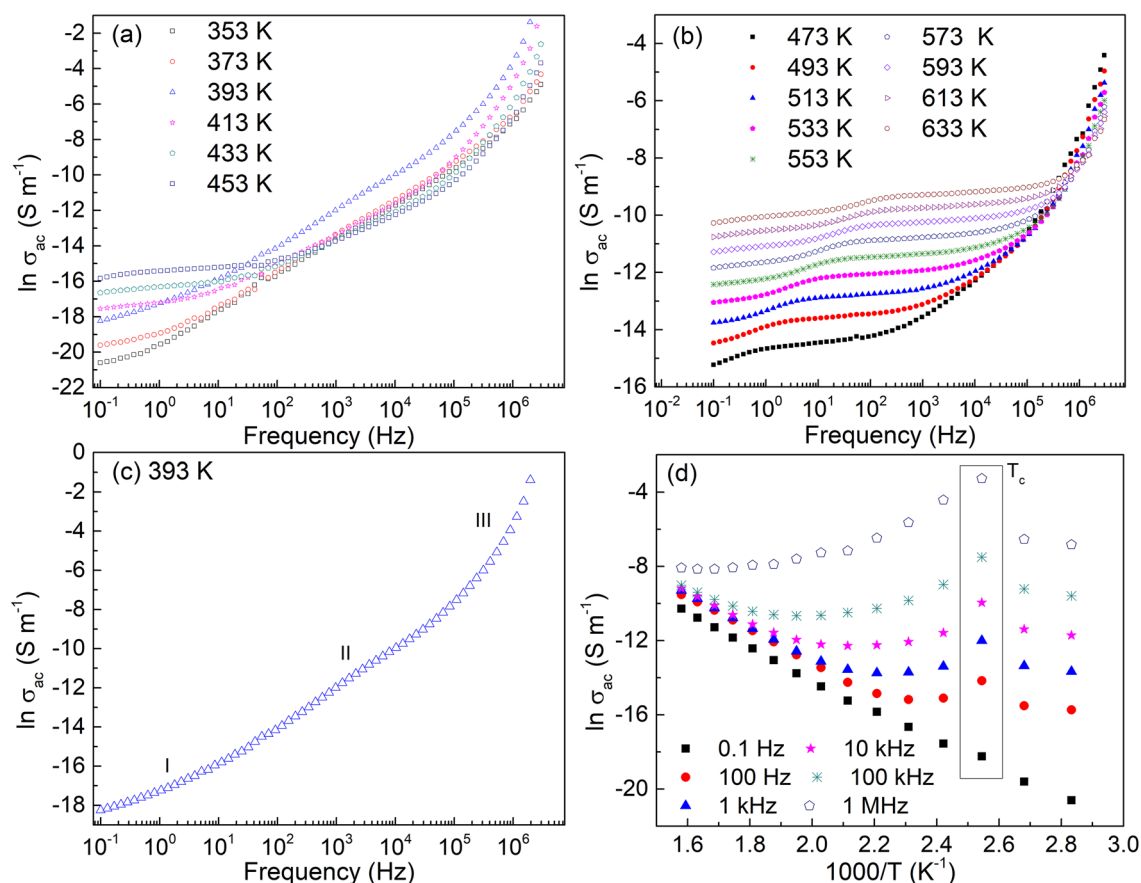


Fig. 10 **a** Frequency dependence of the ac conductivity (σ_{ac}) at different temperatures, **b** variation of σ_{ac} at several temperatures, **c** a typical σ_{ac} spectrum at 393 K, **d** σ_{ac} versus the inverse of temperature at different frequencies above and below the Curie temperature (T_c)

and 1 MHz at higher temperatures. The activation energy of singly ionized, doubly ionized and diffusion of oxygen vacancies lies in the range of 0.1–0.5, 0.6–1.2, and ~ 1.0 eV, respectively [21]. Hence, the obtained values of activation energy suggest that in the ferroelectric region, at low frequency, electron thermal excitation is possibly governed by doubly ionized oxygen vacancies.

In summary, in the operating temperature range of BCT (below ~ 400 K), conductivity exhibits almost linear behavior. In the ferroelectric temperature region, it is found that the doubly ionized oxygen vacancies govern the conduction mechanism with a localized relaxation process and no hopping of electron is observed. Although mobile charges and other defects are present in the material, they do not contribute extensively to the operational temperature range of interest. Therefore, it can be said that at low temperatures, BCT demonstrates highly resistive behavior, as shown in Fig. 3. Thus, the bulk response cannot translate to a high loss contribution. In this temperature range, the major losses are associated with the phase transition. In conclusion, BCT exhibits highly resistive behavior which reduces the leakage

current or pyroelectric loss and improves the pyroelectric properties.

3.6 Pyroelectric analysis

BCT has been identified to exhibit potential for applications in energy harvesting and sensor-based applications. To this end, the pyroelectric voltage is measured by heating/cooling cycles (10–15 cycles) below the Curie temperature T_c (~ 10 – 20 K below T_c). Poling is done using a dc field of 3.0 kV/mm for 1 h at room temperature and subsequently, the pyroelectric voltage was measured using a customized setup shown in Fig. 11a. The sample was aged for 24 h before the pyroelectric measurement was performed. Poled pyroelectric materials were exposed to the temporal temperature gradient to measure the voltage signal. The sample dimension was 25 mm in diameter and 1 mm thick. The pyroelectric material generates a continuous electrical signal upon exposure to a transient thermal gradient. Voltage signals from such a setup do not correspond to the primary pyroelectric response, as bulk samples undergo non-uniform heating along the thickness. Moreover, the voltage output

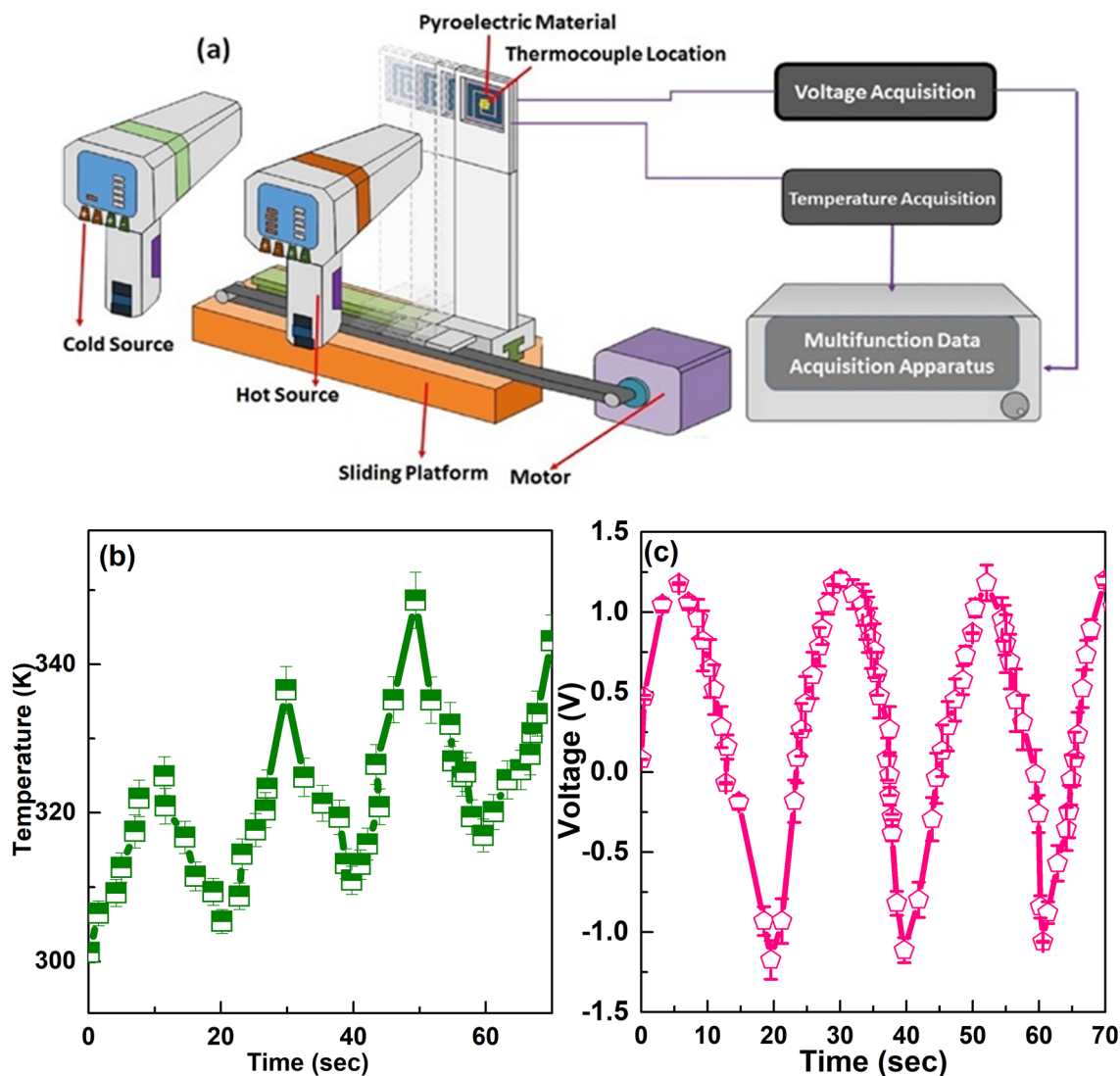


Fig. 11 **a** Schematic of cyclic heating/cooling of the material using hot and cold air, **b** temperature profile on the surface of the material during cyclic heating/cooling, **c** open-circuit voltage (V_{OC}) versus time

from such a system is a cumulative effect of primary and secondary effects [39]. However, such systems are closer to real-time applications. They have been used to investigate energy harvesting possibilities using pyroelectric materials by many researchers [40–45] and hence used in the present investigation.

Figure 11b presents the measured temperature variation near the sample surface as a function of time for a constant frequency (heating/cooling cycles). The open-circuit voltage (V_{OC}) was measured by subjecting the material to continuous thermal cycles for a fixed time interval, as shown in Fig. 11c. It can be seen that the generated voltage signal varies between positive to negative values cyclically on heating/cooling of a pyroelectric ceramic sample. The peak open-circuit voltage was recorded for all compositions and found to be ~ 1.2 V. This

estimation of voltage also depends on other factors like optimum heating/cooling (thermal) cycles. The obtained values in BCT compositions were quite high when compared with traditional pyroelectric ceramics such as $Sr_{0.5}Ba_{0.5}Nb_2O_6$ (SBN) and $Ba_{0.85}Ca_{0.15}Zr_{0.1}Ti_{0.9}O_3$ (BCT–BZT) that demonstrated peak V_{OC} of ~ 0.6 V and ~ 0.7 V, respectively [13]. These results support the possible use of BCT ceramics in pyroelectric applications.

4 Conclusions

BCT ceramics were investigated to establish the conductivity mechanism and explore their potential in energy harvesting applications. In the BCT, two types of relaxation processes

are present which reflect the grain and grain boundary process with a negative temperature coefficient of resistance behavior. The impedance and modulus analysis indicates that BCT exhibits a non-Debye relaxation process. In the ferroelectric state, the conduction mechanism is mainly associated with oxygen vacancies and shows a localized relaxation process. BCT is highly resistive in the low-temperature region and hence, the bulk response cannot translate to a high loss contribution. In the ferroelectric state, higher losses accompany the phase transition. The pyroelectric voltage is 1.2 V and is approximately twice that of BCT–BZT.

Acknowledgements S Patel acknowledges K.S. Srikanth and Dr. Rahul Vaish for providing the sample and materials characterization from the School of Engineering, Indian Institute of Technology Mandi. S Patel also acknowledges Sebastian Steiner from the Department of Materials and Earth Sciences, Technische Universität Darmstadt, Germany, for assistance with measuring the impedance dataset and interpreting the results.

Compliance with ethical standards

Conflict of interest The authors declare that they have no known competing financial interests or personal relationships that could have appeared to influence the work reported in this paper.

References

1. K. Uchino, *Ferroelectric Devices* (CRC Press, New York, 2009).
2. J.F. Tressler, S. Alkoy, R.E. Newnham, *J. Electroceram.* **2**(4), 257–272 (1998)
3. J. Rödel, W. Jo, K.T. Seifert, E.M. Anton, T. Granzow, D. Damjanovic, *J. Am. Ceram. Soc.* **92**(6), 1153–1177 (2009)
4. M. Acosta, N. Novak, V. Rojas, S. Patel, R. Vaish, J. Koruza, G.A. Rossetti Jr., J. Rödel, *Appl. Phys. Rev.* **4**(4), 041305 (2017)
5. G.H. Haertling, *J. Am. Ceram. Soc.* **82**(4), 797–818 (1999)
6. W. Liu, X. Ren, *Phys. Rev. Lett.* **103**(25), 257602 (2009)
7. G. Brennecke, R. Sherbondy, R. Schwartz, J. Ihlefeld, *Ferroelectricity—A revolutionary century of discovery.* *Am. Ceram. Soc. Bull.* **99**(1), 24–30 (2020)
8. A.J. Bell, O. Deubzer, *MRS Bull.* **43**(8), 581–587 (2018)
9. J. Koruza, L. Kodumudi Venkataraman, B. Malič. in Stojanovic BD (ed) *Magnetic, Ferroelectric, and Multiferroic Metal Oxides. Chapter 3 Leadfree perovskite ferroelectrics.* Elsevier, Amsterdam (2018)
10. K. Hayashi, E. Aikawa, T. Ueno, T. Kajitani, Y. Miyazaki, *Phys. Status Solidi A* **215**(11), 1870023 (2018)
11. V.H. Le, N. Van Khien, T. Van Chuong, *Mater. Trans.* **56**(9), 1374–1377 (2015)
12. X.N. Zhu, W. Zhang, X.M. Chen, *AIP Adv.* **3**(8), 082125 (2013)
13. A. Kumar, R. Vaish, S. Kumar, V.P. Singh, M. Vaish, V. Singh Chauhan, K.S. Srikanth, *Energy Technol.* **6**(5), 943–949 (2018)
14. K.S. Srikanth, M.K. Hooda, H. Singh, V.P. Singh, R. Vaish, *Mater. Sci. Semicond. Process.* **79**, 153–160 (2018)
15. M. Sharma, S. Patel, V. Singh, R. Vaish, *J. Appl. Phys.* **128**(9), 095108 (2020)
16. K. Feliksik, L. Kozielski, I. Szafraniak-Wiza, T. Goryczka, M. Adamczyk-Habrajska, *Materials* **12**(24), 4036 (2019)
17. S.-H. Yoon, S.-H. Kang, S.-H. Kwon, K.-H. Hur, *J. Mater. Res.* **25**(11), 2135–2142 (2010)
18. A. Salhi, S. Sayouri, A. Alimoussa, L. Kadira, *Mater. Today Proceed.* **13**, 1248–1258 (2019)
19. L. Kadira, S. Sayouri, A. Elmesbahi, A. Salhi, *Mater. Today Proceed.* **13**, 1238–1247 (2019)
20. P. Victor, R. Ranjith, S. Krupanidhi, *J. Appl. Phys.* **94**(12), 7702–7709 (2003)
21. T. Mondal, S. Das, T. Badapanda, T. Sinha, P. Sarun, *Phys. B* **508**, 124–135 (2017)
22. M.A. Rafiq, M.N. Rafiq, K.V. Saravanan, *Ceram. Int.* **41**(9), 11436–11444 (2015)
23. A. Kaushal, S.M. Olhero, B. Singh, D.P. Fagg, I. Bdkin, J.M.F. Ferreira, *Ceram. Int.* **40**(7 Part B), 10593–10600 (2014)
24. S. Kumar, K. Varma, *Curr. Appl. Phys.* **11**(2), 203–210 (2011)
25. A.K. Jonscher, *J. Phys. D Appl. Phys.* **32**(14), R57 (1999)
26. B. Evgenij, M.J. Ross, *Impedance Spectroscopy: Theory, Experiment, and Applications* (Wiley, Hoboken, 2005).
27. K. Sambasiva Rao, D. Madhava Prasad, P. Murali Krishna, B. Tilak, K.C. Varadarajulu, *Mater. Sci. Eng. B* **133**(1), 141–150 (2006)
28. T. Mondal, B.P. Majee, S. Das, T.P. Sinha, T.R. Middy, T. Badapanda, P.M. Sarun, *Ionics* **23**(9), 2405–2416 (2017)
29. F.D. Morrison, D.C. Sinclair, A.R. West, *J. Am. Ceram. Soc.* **84**(3), 531–538 (2001)
30. A. Molak, M. Paluch, S. Pawlus, J. Klimontko, Z. Ujma, I. Gruszka, *J. Phys. D Appl. Phys.* **38**(9), 1450–1460 (2005)
31. A.K. Roy, A. Singh, K. Kumari, K. Amar Nath, A. Prasad, K. Prasad, *ISRN Ceram.* **2012**, 1–10 (2012)
32. R. Ranjan, R. Kumar, N. Kumar, B. Behera, R. Choudhary, *J. Alloys Compd.* **509**(22), 6388–6394 (2011)
33. S.P. Singh, A.K. Singh, D. Pandey, H. Sharma, O. Parkash, *J. Mater. Res.* **18**(11), 2677–2687 (2003)
34. J. Joshi, D. Kanchan, M. Joshi, H. Jethva, K. Parikh, *Mater. Res. Bull.* **93**, 63–73 (2017)
35. J. Joshi, K. Dixit, M. Joshi, K. Parikh. *AIP Conference Proceedings.* AIP Publishing LLC (2016)
36. J.M. Réau, S. Rossignol, B. Tanguy, J.M. Rojo, P. Herrero, R.M. Rojas, J. Sanz, *Solid State Ion.* **74**(1), 65–73 (1994)
37. K.P. Padmasree, D.K. Kanchan, A.R. Kulkarni, *Solid State Ion.* **177**(5), 475–482 (2006)
38. S. Pattanayak, R. Choudhary, P.R. Das, S. Shannigrahi, *Ceram. Int.* **40**(6), 7983–7991 (2014)
39. S. Jachalke, E. Mehner, H. Stöcker, J. Hanzig, M. Sonntag, T. Weigel, T. Leisegang, D. Meyer, *Appl. Phys. Rev.* **4**(2), 021303 (2017)
40. Q. Leng, L. Chen, H. Guo, J. Liu, G. Liu, C. Hu, Y. Xi, *J. Mater. Chem. A.* **2**(30), 11940–11947 (2014)
41. D. Guyomar, G. Sebald, E. Lefeuvre, A. Khodayari, *J. Intell. Mater. Syst. Struct.* **20**(3), 265–271 (2009)
42. S.H. Krishnan, D. Ezhilarasi, G. Uma, M. Umamathy, *IEEE Trans. Sustain. Energy* **5**(1), 73–81 (2014)
43. P. Mane, J. Xie, K.K. Leang, K. Mossi, *IEEE Trans. Ultrason. Ferroelectr. Freq. Control.* **58**(1), 10–17 (2011)
44. U. Erturun, C. Green, M.L. Richeson, K. Mossi, *J. Intell. Mater. Syst. Struct.* **25**(14), 1838–1849 (2014)
45. C.-C. Hsiao, J.-W. Jhang, A.-S. Siao, *Energies* **8**(7), 7465–7477 (2015)

Publisher's Note Springer Nature remains neutral with regard to jurisdictional claims in published maps and institutional affiliations.